

Prospects for measuring the Doppler magnification dipole with LSST and DESI

Isabelle Ye ,¹★ Philip Bull ,^{1,2} Caroline Guandalin ,³ Chris Clarkson ,^{2,4} Ainulnabilah Nasirudin ,¹

¹Jodrell Bank Centre for Astrophysics, University of Manchester, Manchester M13 9PL, UK

²Department of Physics and Astronomy, University of Western Cape, Cape Town 7535, South Africa

³Institute for Astronomy, University of Edinburgh, Royal Observatory, Blackford Hill, Edinburgh EH9 3HJ, UK

⁴School of Physical and Chemical Sciences, Queen Mary University of London, London, UK

Accepted XXX. Received YYY; in original form ZZZ

ABSTRACT

We forecast the detectability of the Doppler magnification dipole with a joint analysis of galaxy spectroscopic redshifts and size measurements. The Doppler magnification arises from an apparent size variation caused by galaxies' peculiar velocities when mapping them from redshift space to real space. This phenomenon is the dominant contribution to the convergence at low redshifts ($\lesssim 0.5$). A practical observational strategy is to cross-correlate a galaxy number count tracer, e.g. from the Dark Energy Spectroscopic Instrument (DESI) Bright Galaxy Survey, with the convergence field reconstructed from galaxy size measurements obtained by the Vera C. Rubin Observatory's Legacy Survey of Space and Time (LSST). To assess the achievable precision of galaxy size measurements, we simulate LSST Y1-quality galaxy images with GALSIM and measure them with the GALIGHT profile fitting package. Our investigations, based on galaxy populations from LSST's synthetic galaxy catalogue cosmoDC2, show that the variance due to intrinsic galaxy size variation dominates over size measurement errors as expected, but may be lower than previous studies have suggested. Under our analysis assumptions, the Doppler magnification dipole would be detectable with a signal-to-noise ratio ≥ 10 in multiple redshift bins between $0.1 \leq z \leq 0.5$ with DESI spectroscopic redshifts and LSST imaging.

Key words: (cosmology:) large-scale structure of Universe

1 INTRODUCTION

Peculiar velocities are the motions of galaxies driven by gravitational forces from nearby structures, separate from the apparent velocity associated with the homogeneous and isotropic cosmic expansion described by Hubble's law. These deviations from the Hubble flow trace the growth of large-scale structure and the underlying matter distribution (e.g. Gorski et al. 1989; Feldman et al. 2010; Koda et al. 2014; Turner 2024), and are therefore a valuable cosmological probe that allows us to test General Relativity and its possible alternatives (e.g. Hellwing et al. 2014; Ivarsen et al. 2016; Lyall et al. 2023). Since a galaxy's peculiar motion along the line of sight contributes an extra Doppler shift to its observed redshift, measuring this velocity requires an independent estimate of the galaxy's distance to infer the expected Hubble flow redshift at that location. In practice, this is commonly achieved by using redshift-independent distance indicators such as Type Ia supernovae (Phillips 1993), scaling relations such as the Tully-Fisher relation (Tully & Fisher 1977) for spiral galaxies or the Fundamental Plane (Djorgovski & Davis 1987; Dressler et al. 1987) for ellipticals, and even gravitational wave events (Holz & Hughes 2005). Statistically, in galaxy redshift surveys, it can also be measured by the redshift-space distortion (RSD) through characteristic anisotropies in the clustering of galaxies (Kaiser 1987).

A less direct but powerful consequence of galaxy peculiar mo-

tions is the Doppler magnification effect (Bonvin 2008; Bacon et al. 2014). It arises from peculiar velocities shifting galaxy locations in redshift space, causing shifts in their apparent flux and angular size as a function of observed redshift. This redshift-size mismatch induces an apparent lensing convergence and magnification signal. At fixed observed redshift, galaxies that are actually moving toward the observer appear fainter and smaller than naively expected, while those receding appear brighter and larger than they would have done if their observed redshift were equal to their true cosmological redshift. Around an overdensity, this generates a dipolar magnification pattern, as near-side infalling galaxies appear magnified and far-side receding ones are demagnified (Bacon et al. 2014).

Over the past decade, a number of studies have built the theoretical foundation for Doppler magnification as a cosmological probe. The effect was first highlighted by Bonvin (2008), who noted that the galaxy's velocity would induce an apparent magnification of its image. Subsequent works showed that at low redshifts, this Doppler-induced magnification can dominate over the gravitational lensing signal (Bacon et al. 2014; Bonvin et al. 2017; Coates et al. 2021; Bonvin et al. 2023). Bacon et al. (2014) introduced the term "Doppler lensing" and used simulations to demonstrate that a high signal-to-noise ratio (SNR) detection could be achieved with upcoming surveys. Based on these insights, Bonvin et al. (2017) developed a practical estimator to isolate the Doppler magnification dipole signal, by extracting the dipole term in the cross-correlation between galaxy number counts and convergence. This estimator largely can-

★ E-mail: isabelle.ye@postgrad.manchester.ac.uk

cells symmetric lensing contributions up to $z \sim 0.5$, thereby providing a cleaner measurement. The predicted dipole signal is strongest at low redshifts where peculiar velocities can be a significant contribution to the observed redshift. This is a direct way to trace the galaxy peculiar velocity field, and is an independent probe of the growth rate that complements more traditional RSD measurements (e.g., Zarrouk et al. 2018; Icaza-Lizola et al. 2020).

The number count of galaxies is a well-studied observable (Bonvin & Durrer 2011; Challinor & Lewis 2011), but using galaxy sizes to infer convergence is less explored. Galaxy size estimates are a by-product of weak lensing surveys, which tend to focus on the shear signal by measuring galaxy ellipticities. Casaponsa et al. (2013) showed that unbiased estimates of the convergence field (and thus cosmic size magnification) can be extracted from galaxy samples provided that the galaxies have angular sizes larger than the point spread function (PSF) and have high SNR (> 10). Similarly, Alsing et al. (2015) offered a Bayesian methodology for estimating the convergence field based on galaxy angular size and flux measurements. These studies established the observational viability of using the galaxy distribution and sizes as a probe of lensing convergence (and thus the Doppler magnification signal).

Andrianomena et al. (2019) presented encouraging forecasts for surveys carried out with the Dark Energy Spectroscopic Instrument (DESI; DESI Collaboration et al. 2022) and the futuristic Square Kilometre Array (SKA) Phase 2 with the 21cm line, finding that they could detect the Doppler magnification dipole with high SNR. Such measurements could be used to test cosmological models and modifications to General Relativity on large scales, and would provide a useful alternative to other observables as this peculiar velocity lensing probe is sensitive to different systematics than standard methods. More recently, Coates et al. (2021) employed a fully relativistic N -body simulation to verify that the Doppler magnification term in the lensing convergence can be recovered as predicted by relativistic perturbation theory. In addition, Bonvin et al. (2023) split a galaxy sample by luminosity (into ‘‘bright’’ and ‘‘faint’’ subsamples) and forecast a detectable $\sim 20\sigma$ dipole in the two-point correlation function using DESI’s Bright Galaxy Survey (BGS; Hahn et al. 2023).

Galaxy size magnification due to the Doppler effect is a subtle signal, and has not yet been detected. However, with upcoming surveys like the Legacy Survey of Space and Time (LSST; Ivezić et al. 2019) and DESI, it is important to further assess its detectability, while also taking into account realistic observational complications such as the PSF and detector effects. In this work, we extract DESI BGS-like samples from a realistic LSST mock galaxy catalogue, investigate the intrinsic galaxy size variations, simulate LSST-like images, and measure galaxy sizes to quantify the measurement uncertainties. Finally, we forecast the expected SNR for the dipole in joint DESI+LSST observations.

This paper is structured as follows. In Section 2, we describe the theory of Doppler magnification, focusing on the dipole component of the two-point function, along with the corresponding estimator and its variance. In Section 3, we present the DESI-like sample selection from the cosmoDC2 simulated catalogue (Korytov et al. 2019), quantify the intrinsic galaxy size variations, and use simulated LSST-like images to assess measurement uncertainties, yielding the total per-bin uncertainty on the convergence used in our forecasts. In Section 4, we present the forecast dipole amplitude and SNR in four redshift bins, and in Section 5 we discuss and conclude.

In what follows, we assume a Planck cosmology with $\Omega_c = 0.261$, $\Omega_b = 0.0490$, $h = 0.677$, $\sigma_8 = 0.811$, $n_s = 0.965$, and $N_{\text{eff}} = 3.046$ (Planck Collaboration et al. 2020).

2 THEORY

In this section, we outline the theoretical framework for Doppler magnification. We first define the number count contrast and lensing convergence, then describe how the Doppler magnification dipole can be extracted using cross-correlations. We then present expressions for the variance and measurement uncertainties.

2.1 The Doppler magnification dipole

The galaxy number count contrast Δ is defined as the fractional excess of galaxy counts in a direction \mathbf{n} at redshift z relative to the mean:

$$\Delta(\mathbf{n}, z) = \frac{N(\mathbf{n}, z) - \langle N(z) \rangle}{\langle N(z) \rangle}, \quad (1)$$

where $N(\mathbf{n}, z)$ is the number of galaxies in a given volume element at observed redshift z in the direction \mathbf{n} (defined from the observer to the source), and $\langle N \rangle$ is the mean number of galaxies over a sufficiently large volume. Regions where $\Delta > 0$ are considered overdense, while regions with $\Delta < 0$ are underdense. At linear order, the number count contrast can be approximated as a sum of density and velocity contributions (see e.g. Andrianomena et al. 2019):

$$\Delta(\mathbf{n}, z) \simeq b\delta - \frac{1}{\mathcal{H}} \partial_r(\mathbf{V} \cdot \mathbf{n}), \quad (2)$$

where b is the linear galaxy bias, δ is the matter density contrast, $\mathcal{H} \equiv aH$ is the conformal Hubble parameter, with a the scale factor, H is the expansion rate, r is the comoving distance to the galaxy, and $\mathbf{V} \cdot \mathbf{n}$ is the line-of-sight component of the galaxy peculiar velocity field. Full expressions at linear order, including terms neglected above, can be found in Bonvin & Durrer (2011); Challinor & Lewis (2011).

The lensing convergence κ quantifies the fractional change (magnification or demagnification) in the apparent surface area of a background galaxy. It receives contributions from several effects: the gravitational convergence κ_g (the standard weak gravitational lensing term), the Doppler convergence κ_v , the Sachs-Wolfe term κ_{SW} and the Integrated Sachs-Wolfe term κ_{ISW} . The last two terms (κ_{SW} and κ_{ISW}) are generally very small compared to κ_g and κ_v and are typically neglected (Bacon et al. 2014). We therefore consider $\kappa \simeq \kappa_g + \kappa_v$ for our analysis.

The Doppler convergence κ_v arises from line-of-sight peculiar velocities shifting the observed redshift, and thus the apparent magnification can be influenced by both the foreground and background structures. Its contribution can be written as (Bonvin 2008; Bacon et al. 2014; Andrianomena et al. 2019)

$$\kappa_v = \left(\frac{c}{r\mathcal{H}} - 1 \right) \frac{\mathbf{V} \cdot \mathbf{n}}{c}. \quad (3)$$

If a galaxy is moving towards the observer (i.e., $\mathbf{V} \cdot \mathbf{n} < 0$), then $\kappa_v < 0$, the galaxy is demagnified, and its observed angular size appears smaller. Its flux, evaluated at fixed observed redshift z_{obs} , is dimmer than if it had no peculiar motion. Conversely, for a galaxy moving away, it appears magnified. This differential effect produces a characteristic dipole pattern – a spatial anisotropy pattern in the observed galaxy distribution around overdensities.

Importantly, at low redshifts the Doppler magnification dominates over the gravitational lensing magnification. At $z \lesssim 0.45$, the Doppler term κ_v exceeds the gravitational term κ_g , so that κ_g can be safely neglected when extracting the dipole signal (Bacon et al. 2014; Bonvin et al. 2017).

We can estimate κ using a Bayesian approach (Alsing et al. 2015). This method constructs a posterior distribution for κ by incorporating prior knowledge of the intrinsic distribution of galaxy sizes and

magnitudes, along with a model describing how lensing modifies these observables. The lensing convergence κ affects the logarithm of the observed galaxy size – here the size is defined as $\sqrt{\text{Area}}$, and $\lambda = \ln \sqrt{\text{Area}}$ – and affects the magnitude m linearly:

$$\lambda_{\text{obs}} = \lambda_{\text{int}} + \kappa, \quad m_{\text{obs}} = m_{\text{int}} - q\kappa, \quad (4)$$

where $q = -5 \log_{10} e \approx -2.17$, the subscript ‘‘obs’’ refers to the observed value and ‘‘int’’ refers to the galaxy’s intrinsic (unlensed) value. In what follows, we will adopt the half-light radius R as a proxy for the galaxy size, such that $\lambda \approx \ln R$. The main factors that determine how well we can estimate κ for each galaxy are the measurement noise in galaxy size and flux, and the intrinsic dispersion in galaxy sizes.

[Bonvin et al. \(2017\)](#) and [Andrianomena et al. \(2019\)](#) developed a formalism that optimally extracts the dipolar modulation induced by Doppler magnification from the cross-correlation between the galaxy number counts and convergence. The two-point cross-correlation function of Δ and κ is given by

$$\xi^{\Delta\kappa} = \langle \Delta(z, \mathbf{n}) \kappa(z', \mathbf{n}') \rangle, \quad (5)$$

where (z, \mathbf{n}) and (z', \mathbf{n}') denotes the redshift and line-of-sight direction at which Δ and κ are evaluated, respectively.

One can use the following estimator to extract the dipole directly from survey data ([Bonvin et al. 2017](#)):

$$\hat{\xi}_{\text{dipole}}^{\Delta\kappa}(d) = a_N \sum_{ij} \Delta_i \kappa_j \cos \beta_{ij} \delta_{d_{ij}, d}^K. \quad (6)$$

Here, $a_N = 3 l_p^5 / (4\pi V d^2)$ is a normalisation factor that depends on the cell size l_p of the cubic grid which the fields are discretised onto for the correlation function measurement, and on the comoving volume V of a redshift bin centred at z with width Δz . The indices i and j denote voxels in the survey separated by comoving distance d_{ij} , which are summed over all ij pairs. The quantity β_{ij} is the angle between the separation vector d_{ij} that connects Δ to κ and the line-of-sight direction at the position where Δ is measured (see Figure 1 of [Andrianomena et al. 2019](#)). The Kronecker delta function implements the binning in separation, d .

The dipole component of the two-point function for Δ and κ_ν may be computed theoretically as ([Andrianomena et al. 2019](#))

$$\xi_{\text{dipole}}^{\Delta\kappa_\nu} \simeq \frac{1}{2\pi^2} \left(1 - \frac{1}{\mathcal{H}r}\right) \left(\lambda_1 + \frac{4}{15} \nu_1\right) P_1(\cos \beta), \quad (7)$$

where P_1 is the Legendre polynomial of degree 1. The functions λ_1 and ν_1 are given by

$$\begin{aligned} \lambda_1(d, r, \beta) &= \int dk k^2 j_1(kd) \mathcal{G}(z', k) T^2(k) \mathcal{P}(k) \\ &\times \left[\frac{2b}{3\Omega_m} \left(\frac{k}{\mathcal{H}_0} \right)^2 D(z, k) + \frac{1}{3} \frac{k}{\mathcal{H}(z)} \mathcal{G}(z, k) \right], \end{aligned} \quad (8)$$

and

$$\nu_1(d, r, \beta) = \int dk k^2 j_1(kd) T^2(k) \mathcal{P}(k) \frac{k}{\mathcal{H}(z)} \mathcal{G}(z, k) \mathcal{G}(z', k), \quad (9)$$

where j_1 is the spherical Bessel function with $\ell = 1$; $\mathcal{P}(k)$ is the (dimensionful) primordial power spectrum, defined in terms of the primordial gravitational potential perturbation Ψ_p as $\langle \Psi_p(k) \Psi_p(k') \rangle = (2\pi)^3 \mathcal{P}(k) \delta^D(k + k')$; $D(z, k)$ is the growth factor of the matter density perturbations, normalised as $D(a = 1, k) = 1$; $T(k)$ is the Λ CDM matter transfer function, and

$$\mathcal{G}(a, k) = \frac{2k \mathcal{H}}{3 \mathcal{H}_0^2 \Omega_m} f D \quad (10)$$

is the velocity growth factor, where Ω_m is the fractional matter density at $z = 0$, and $f \equiv d \ln D / d \ln a$ is the logarithmic growth rate.

Following Equation 7.8 from [Dodelson & Schmidt \(2020\)](#), we write, in Equations 8 and 9,

$$\mathcal{P}(k) T^2(k) = \frac{25}{9} \frac{\Omega_m^2 H_0^4}{k^4 c^4 D^2(a)} P_m(k, a), \quad (11)$$

where $P_m(k, a)$ is the matter power spectrum.

2.2 Variance of the dipole estimator

The covariance matrix for the Doppler magnification dipole estimator was also computed by [Andrianomena et al. \(2019\)](#), and is given by

$$\text{cov}[\hat{\xi}_{\text{dipole}}^{\Delta\kappa_\nu}] = \Xi_1(z, d, d') + \Xi_2(z, d, d') + \Xi_3(z, d, d'), \quad (12)$$

where the individual terms are given by

$$\begin{aligned} \Xi_1 &= \frac{9}{V} \left(1 - \frac{1}{\mathcal{H}r}\right)^2 \left(\frac{b^2}{5} + \frac{2bf}{7} + \frac{f^2}{9} \right) \\ &\times f^2 \frac{\mathcal{H}}{\pi^2} \int dk P_m^2(k, z) j_1(kd) j_1(kd') \end{aligned} \quad (13)$$

$$\begin{aligned} \Xi_2 &= \frac{9}{2} \sigma_\kappa^2 \frac{l_p^3}{V} \left(\frac{b^2}{3} + \frac{2bf}{5} + \frac{f^2}{7} \right) \\ &\times \frac{1}{\pi^2} \int dk k^2 P_m^2(k, z) j_1(kd) j_1(kd') \end{aligned} \quad (14)$$

$$\Xi_3 = \frac{3}{4\pi} \frac{\sigma_\kappa^2}{\bar{n}V} \left(\frac{l_p}{d} \right)^2 \delta_{d, d'}^K. \quad (15)$$

The first term is the contribution from the cosmic variance of Δ , κ , and their cross-correlation. The second term quantifies the total variance associated with the size measurements σ_κ , which consists of the intrinsic size error and the measurement error. The third term, which depends on the mean number density of galaxies \bar{n} , arises from the impact of shot noise and also depends on σ_κ .

In this work, we use a simplified σ_κ estimation from galaxy sizes. Following [Alsing et al. \(2015\)](#), the transformation of log-size under lensing (ignoring the magnitude effect) is given by $\langle \lambda \rangle \rightarrow \langle \lambda \rangle + \eta_\lambda \kappa$, where $\eta_\lambda = \partial \langle \lambda \rangle / \partial \kappa$ accounts for the boosting of galaxy sizes due to lensing and the shift of smaller sources across size selection boundaries. Assuming no selection effects, $\eta_\lambda = 1$. The estimator for κ is then

$$\hat{\kappa} = (\lambda - \langle \lambda \rangle) / \eta_\lambda. \quad (16)$$

The uncertainty on κ is equal to the scatter in log-size, i.e., $\sigma_\kappa = \sigma_\lambda$. Using standard error propagation, the uncertainty in log-size is related to the uncertainty in radius via $\sigma_\lambda = \sigma_R / R$, thus $\sigma_\kappa = \sigma_R / R$.

2.3 Uncertainty on the dipole measurement

Accurate measurement of the Doppler magnification dipole requires both high-precision redshifts and robust size estimates. Spectroscopic surveys such as DESI minimise redshift uncertainties (e.g. compared with photometric surveys). Potential systematic biases on the reconstructed convergence field are not as well understood however, and could conceivably bias the dipole measurement or impact its SNR.

We assume that the observed convergence κ_{obs} is the sum of the ‘‘true’’ Doppler magnification convergence κ_ν and an additional noise term,

$$\kappa_{\text{obs}} = \kappa_\nu + \epsilon, \quad (17)$$

where ϵ is a random noise term which follows a Gaussian distribution with mean b_κ (the measurement bias) and standard deviation σ_κ ,

$$\epsilon \sim \mathcal{N}(b_\kappa, \sigma_\kappa). \quad (18)$$

The standard deviation σ_κ includes two contributions: an intrinsic term $\sigma_{\kappa, \text{intrinsic}}$ arising from variations in galaxy sizes and a measured term $\sigma_{\kappa, \text{measured}}$ accounting for uncertainties in size measurement, which are assumed independent and so can be added in quadrature as

$$\sigma_\kappa^2 = \sigma_{\kappa, \text{intrinsic}}^2 + \sigma_{\kappa, \text{measured}}^2. \quad (19)$$

We define the effective σ_κ as the weighted variance averaged over all selected galaxies in the survey,

$$\sigma_\kappa^2 = \frac{\int dm_r dR dz n(m_r, R, z) \sigma_\kappa^2(m_r, R, z)}{\int dm_r dR dz n(m_r, R, z)}, \quad (20)$$

where $n(m_r, R, z)$ is defined as

$$n(m_r, R, z) = \frac{dN}{dV dm_r dR}, \quad (21)$$

dV is the comoving volume element, and m_r is the r -band apparent magnitude. $\sigma_\kappa^2(m_r, R, z)$ is the expected variance of the convergence measurement for a galaxy with m_r, R, z , which can be decomposed into the intrinsic scatter and the measurement error.

3 PROPERTIES OF THE GALAXY SAMPLE

In this section, we describe the selection of a galaxy sample to examine the number count distribution defined in Eq. 21 and other properties. Galaxies are selected from the cosmoDC2 catalogue based on the target selection criteria of the DESI Bright Galaxy Survey (BGS). cosmoDC2 is a comprehensive simulated galaxy catalogue developed for LSST to support precision cosmology (Korytov et al. 2019). It is based on the (4.225 Gpc)³ Outer Rim N -body simulation run and covers a sky area of 440 deg² up to a redshift of $z = 3$. The catalogue reaches a depth of 28 mag in the r band, and includes a rich set of galaxy properties. Its construction combines semi-analytic galaxy formation modelling with empirical calibration. The semi-analytic component is based on the Galacticus model (Benson 2012), which models key baryonic processes such as gas cooling, star formation, and feedback. Additional empirical modelling is applied to reproduce observed relations, including the colour-magnitude and size-luminosity distributions (Korytov et al. 2019).

Galaxy sizes in cosmoDC2 are modelled by separately parameterizing disk and bulge half-light radii using the functional form of Zhang & Yang (2019). These relations are calibrated to SDSS galaxies at $z \approx 0$ and evolve with redshift through a simple scaling that decreases the characteristic sizes by roughly a factor of two at $z = 1$. While the model ensures broad consistency with observed size-luminosity trends, the simulated galaxies are statistically realistic but physically simplified. The simulated galaxy size distribution does not necessarily reproduce that observed in real data in full; however, it provides a statistically consistent and physically plausible framework that is suited for this simulated analysis.

3.1 Selection functions

Given that the dipole signal we aim to measure is intrinsically quite small, spectroscopic redshifts are preferred over photometric estimates due to their reduced uncertainties. We therefore propose using DESI spectroscopic data to construct the number count contrast field

Δ . To characterize the expected galaxy sample, we select galaxies from cosmoDC2 according to the BGS target selection criteria.

While the DESI Peculiar Velocity (PV) Survey (Douglass 2023; Saulder et al. 2023) and the LOW-z Secondary Target Programme (Darragh-Ford et al. 2023) were also considered, they are not suited to detecting the Doppler signal. The PV sample, although scientifically valuable for other peculiar velocity measurements (e.g. using the fundamental plane and the Tully-Fisher relations), has a much lower number density and covers only a limited redshift range ($z \approx 0.05 - 0.15$). Similarly, the LOW-z sample targets galaxies at $z < 0.03$, which falls entirely below our analysis threshold. Therefore we focus exclusively on the BGS sample.

To reproduce an equivalent BGS sample from the cosmoDC2 catalogue, we adopt a magnitude cut of $r < 19.5$, along with broad colour cuts of $-1 < (g - r) < 4$ and $-1 < (r - z) < 4$ (Hahn et al. 2023). While official BGS criteria include fibre magnitude cuts to avoid imaging artifacts, these are not simulated in cosmoDC2. The BGS quality cut also requires at least one photometric observation in the g, r, z bands, which the cosmoDC2 catalogue inherently provides. We focus on the BGS Bright sample and exclude the fainter BGS Faint sample ($19.5 < r < 20.175$), as these galaxies might have low fibre flux and higher redshift uncertainty.

Figure 1 presents the distributions of redshift, true half-light radius (of the major axis) and apparent r -band magnitude m_r for the BGS-selected cosmoDC2 galaxy sample. The redshift distribution dN/dz peaks at $z \sim 0.2$, with a tail extending to $z \sim 0.6$. The true half-light radius distribution dN/dR shows that the majority of galaxies have angular sizes below 2 arcsec, with a steep decline at larger radii. We restrict the plotted range to galaxies with $0 < R < 10$ arcsec to exclude the very small number of extreme outliers with very large radii. The apparent r -band magnitude distribution dN/dm_r shows a sharp increase in number counts toward the faint end, and peaks near the selection threshold at $r = 19.5$. Overall, most sources in the BGS sample are concentrated at $z \sim 0.2$, with compact sizes of $R \sim 1$ arcsec, and relatively faint $m_r \sim 18-20$. For the forecast of the measurement of the Doppler magnification dipole, we choose four redshift bins $0.10 \leq z < 0.20$; $0.20 \leq z < 0.30$; $0.30 \leq z < 0.40$; and $0.40 \leq z < 0.50$.

3.2 The intrinsic σ_κ

The convergence field can be estimated from the galaxy sizes and magnitude measurements (Alsing et al. 2015), and the associated error on the convergence, σ_κ , is a key factor influencing the overall noise level in the dipole signal. The total uncertainty in κ arises from two sources: an intrinsic component due to the inherent variation in galaxy sizes, and measurement-related errors (see Eq. 17). By analysing the size distribution of galaxies selected from the simulation, we aim to characterize the expected intrinsic size variation, and thereby anticipate the noise level on the convergence field.

The intrinsic contribution $\sigma_{\kappa, \text{intrinsic}}$, as defined in Equation 20, is the population-weighted average of $\sigma_\kappa^2(m_r, R, z)$ across the survey. Integrating over m_r , R , and z , weighted by the number density from Equation 21, is equivalent to an average over the full selected galaxy population. Therefore, we need to find the expected intrinsic scatter for each (m_r, R, z) bin in our selected population.

From the catalogue, we select a total of 276,578 BGS-like galaxies. To evaluate $\sigma_{\kappa, \text{intrinsic}}^2(m_r, z)$, we bin the galaxy population in the space of apparent r -band magnitude and redshift. Within each grid cell, we compute the σ_κ^2 as $(\text{std}(R)/\bar{R})^2$, where \bar{R} is the true half-light radius. Figure 2 shows the resulting values of σ_κ^2 across all grid cells, with the contour indicating the number density of the

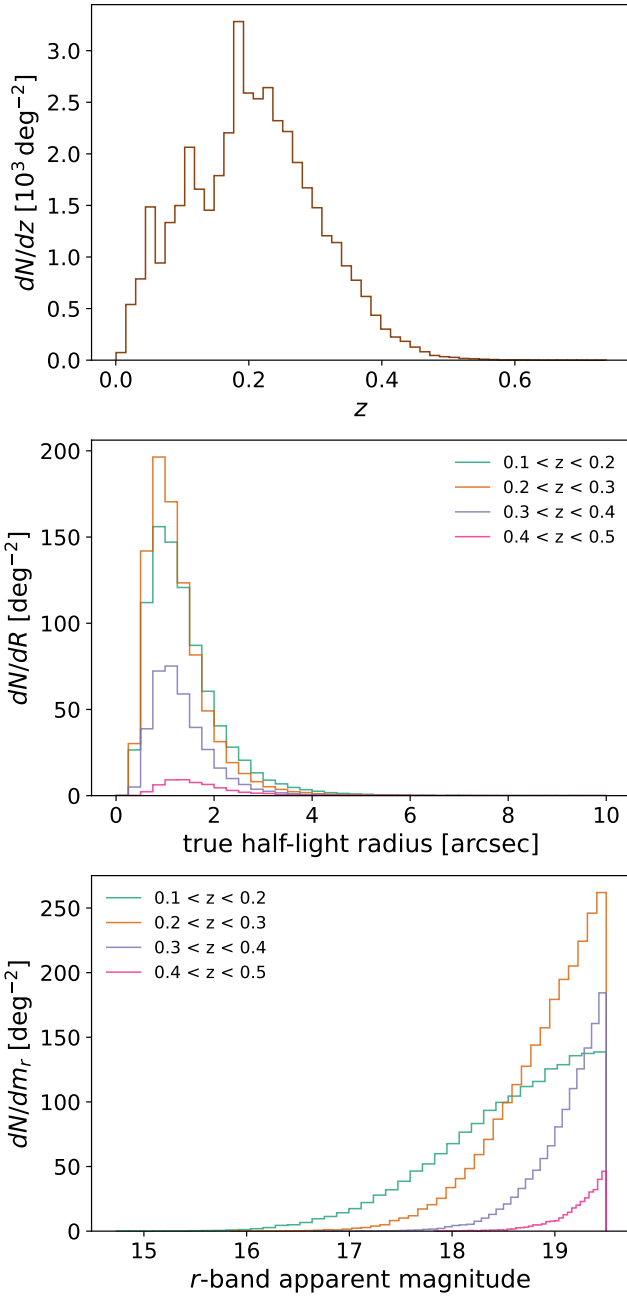


Figure 1. Distributions of galaxy properties from the BGS-selected cosmoDC2 catalogue. Top: redshift distribution of the sample. Middle: true half-light radii (of the major axis) distribution in four redshift bins. Values above 10 arcsec are excluded from the plot for clarity. Bottom: apparent r -band magnitude distribution for the same redshift bins.

galaxies. For each redshift bin in $0.10 \leq z \leq 0.50$, we compute a count-weighted average of σ_κ^2 over all (m_r, z) cells within that bin, yielding an effective value of $\sigma_{\kappa, \text{intrinsic}}$ of the galaxy population at each redshift bin. The results are summarized in Table 1 and visualized in Figure 3. Figure 3 shows the finely binned $\langle \sigma_{\kappa, \text{intrinsic}} \rangle$ as a function of z , averaged over m_r , along with the same quantity computed in the four broad redshift bins as reported in Table 1.

With the 3D-HST+CANDELS sample, van der Wel et al. (2014) found an intrinsic scatter $\sigma_{\log R_{\text{eff}}} \simeq 0.1\text{--}0.14$ for early-type galaxies and $\simeq 0.16\text{--}0.19$ for late-type galaxies over $0 < z < 3$, where we

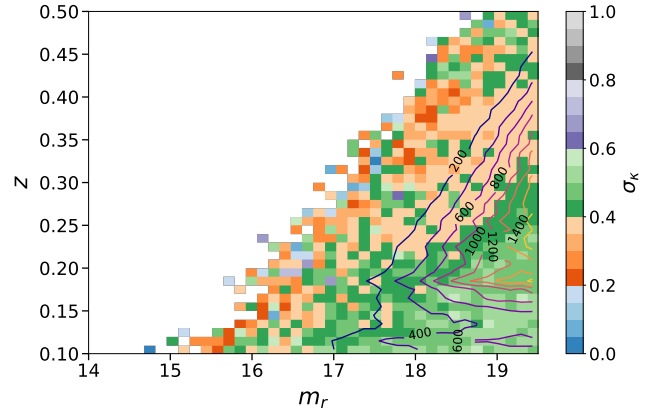


Figure 2. Distribution of $\sigma_{\kappa, \text{intrinsic}}$ in bins of m_r and z for the DESI BGS-like simulated sample selected from the LSST cosmoDC2 simulation. The colour scale represents $\sigma_{\kappa, \text{intrinsic}}$ within each (m_r, z) bin, ranging from 0 to 1, while the contours represent the number of galaxies selected from the catalogue, plotted in intervals of 200.

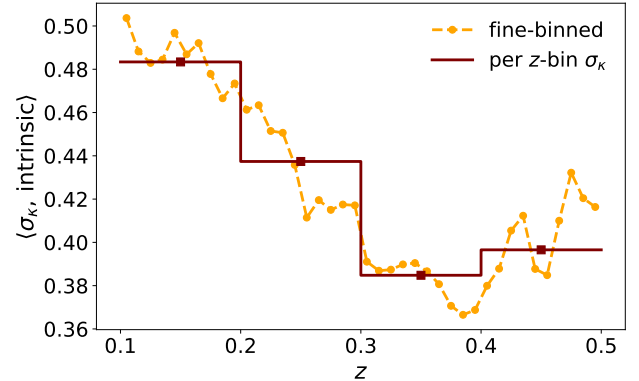


Figure 3. Count-weighted average $\langle \sigma_{\kappa, \text{intrinsic}} \rangle$ in finely binned z intervals and the chosen redshift bins. The orange dashed curve shows the values of the computed $\sigma_{\kappa, \text{intrinsic}}$ from Figure 2 averaged over m_r . The maroon step function shows the average of $\sigma_{\kappa, \text{intrinsic}}$ within the chosen redshift bins, with the square markers at the midpoints of each redshift bin.

have taken these values to be in dex (\log_{10}). At higher redshifts using JWST NIRCam, Allen et al. (2025) measured an intrinsic scatter of $\sigma_{\log R_{\text{eff}}} = 0.188 \pm 0.007$ over $3 < z < 9$, within 1σ agreement with values at lower redshift from van der Wel et al. (2014), where R_{eff} denotes the effective radius. These results suggest that the intrinsic scatter has little to no evolution with redshift. The values found from the simulated catalogue are broadly consistent with these results.¹

3.3 Image simulations

We employ the modular image simulation package GALSIM² (Rowe et al. 2015) to generate galaxy images using simple profiles and properties (such as Sérsic index n , half-light radius R) as well as observational effects such as the point spread function (PSF), detector characteristics and sky background noise. Subsequently, we measure the sizes of the galaxies in these simulated images to assess biases

¹ For reference, we approximate $\sigma_{\log R_{\text{eff}}} = 0.1(0.2)$ as $\sigma_\kappa \approx 0.23(0.48)$.

² <https://github.com/GalSim-developers/GalSim>

z	N_{obj}	$\sigma_{\kappa, \text{measured}}$	$\sigma_{\kappa, \text{intrinsic}}$	$\sigma_{\kappa, \text{total}}$
$0.10 \leq z < 0.20$	2311	0.027	0.48	0.48
$0.20 \leq z < 0.30$	4038	0.032	0.44	0.44
$0.30 \leq z < 0.40$	2443	0.032	0.39	0.39
$0.40 \leq z < 0.50$	666	0.029	0.40	0.40

Table 1. The estimates of the intrinsic and measured σ_{κ} values in four redshift intervals used in our forecasts. For each redshift bin we list the number of simulated galaxies N_{obj} from the set of 10,000 randomly selected BGS-like galaxies (see Section 3.3), the measurement contribution $\sigma_{\kappa, \text{measured}}$ from the image-simulation pipeline (as described in Section 3.4), the intrinsic size dispersion $\sigma_{\kappa, \text{intrinsic}}$ (Equation 20), and their quadrature sum $\sigma_{\kappa, \text{total}}$, which is used in our analysis.

in size recovery across a variety of DESI BGS-like galaxies. This image simulation is set up to mimic the expected data quality of the LSST Year 1 (Y1) observations.

For simulated galaxy images, we randomly selected 10,000 DESI BGS-like galaxies from the cosmoDC2 catalogue. For each selected galaxy, we generate images using true half-light radius, apparent r -band magnitude and redshift from the catalogue. All other input parameters are held fixed except for the random realisation of image CCD noise. The galaxy flux for each image is set by its apparent magnitude, instrumental zero point, and exposure time t_{exp} as

$$F_{\text{gal}} = \frac{t_{\text{exp}}}{\text{gain}} \cdot 10^{-0.4 \cdot (m - Z)}, \quad (22)$$

where F_{gal} is the flux of the galaxy, t_{exp} is the exposure time, m is the apparent magnitude of the galaxy, and Z is the photometric zero point. We adopt $Z = 28.36$ mag, corresponding to the LSST instrumental zero point for a 1-second exposure at unit gain, and a detector gain of 1.6 electrons per ADU.³ The single-visit exposure time is set to 30 seconds (LSST Science Collaboration et al. 2009).

To reduce complexity, we model each galaxy as a single-component system with a Sérsic surface brightness profile and a fixed Sérsic index of $n = 1.5$. This is a simplifying assumption regarding the Sérsic index: early-type elliptical galaxies or bulge components typically have $n \sim 4$ and late-type spiral galaxies or disk components have $n \sim 1$ (e.g., Shen et al. 2003; Lange et al. 2015). Given that most galaxies in our target redshift range ($z \sim 0.1 - 0.5$) are late-type, we consider $n = 1.5$ a reasonable choice. As we discuss later in Section 3.4, we find the measured size error to be much smaller than the intrinsic size error. We also test the extreme case of $n = 4$, and find the same conclusion.

The image pixel scale is set to 0.2 arcsec/pixel, matching the LSST CCD design (Ivezic et al. 2019). Each side of each image stamp has a pixel number equal to 25 times the galaxy's half-light radius divided by the pixel scale. The simulated galaxies are isolated, without nearby stars, galaxies, or otherwise. We do not account for ellipticity in the galaxy models, as the summary statistics we use are averaged over a large number of galaxies. This simplifying assumption effectively treats all the galaxies as viewed face-on. The PSF model includes both atmospheric and optical components, which are convolved to form a total PSF. The atmospheric PSF is modeled with a Kolmogorov profile and a fiducial seeing of 0.7 arcsec (Ivezic et al. 2019). The optical PSF accounts for telescope effects: a wavelength-to-diameter ratio of 0.017, a linear obscuration of 40% of the primary mirror diameter, and four support struts with thickness of 0.03. The struts are oriented at an angle of 10 degrees. Optical aberrations are also

included. Both the optical PSF and the aberration parameters follow the GalSim LSST example configuration.⁴

The simulated noise characteristics include both Poisson (photon) noise and Gaussian read noise. A uniform sky background of 18,000 ADU per arcsec² is added to each image, and the Gaussian read noise is set to 3.4 rms per pixel per read, following the values in the GalSim LSST example configuration. The noise is applied using independent random seeds, ensuring unique noise realisations. To approximate the noise level for the LSST-Y1 coadded image, the noise is scaled by a factor of $1/\sqrt{82.5}$. This is based on the LSST baseline of ~ 825 visits per field over ten years (Jones et al. 2021), and reflects that coadding N independent exposures reduces the noise level by a factor of \sqrt{N} . The full 10-year LSST data quality will benefit from deeper coadds, so the corresponding $\sigma_{\kappa, \text{measured}}$ is expected to be slightly smaller than in this Y1 simulation. A few examples of the simulated galaxy images are presented in Appendix A (Figure A1).

For each simulated galaxy, we generated and archived three types of images: the final galaxy image that is convolved with PSF and noise, the corresponding PSF-only image (i.e. containing only the PSF model, without galaxy or noise), and the noise rms image. These images are the inputs required for size measurements using GALIGHT (see Section 3.4). In real observing scenarios, these components would be provided as estimates based on the full images.

3.4 Size measurement

We used GALIGHT (Ding et al. 2020) to estimate the apparent size of each galaxy from the simulated images. GALIGHT is an open-source python package for two-dimensional image modelling, built on the image modelling capabilities of LENSTRONOMY (Birrer et al. 2021). It provides image processing, PSF handling, and 2D profile fitting for galaxy structural components. In our implementation, the fitting is performed individually for each image. The fitting process incorporates both the PSF and the noise rms map, as saved during the image generation step. We use the shallow fitting level in the fitting process and choose the particle swarm optimization (PSO) algorithm (Kennedy & Eberhart 1995) to maximise the model likelihood.

To characterise the accuracy of our galaxy size measurements, we quantified the measurement error as the mean squared difference between the best-fit and true half-light radii, averaged over the selected 10,000 galaxies:

$$\sigma_{\kappa, \text{measured}}^2 = \left\langle (R_{\text{measured}} - R_{\text{true}})^2 / R_{\text{true}}^2 \right\rangle. \quad (23)$$

We present the measurement uncertainty of galaxy sizes (half-light radius), $\sigma_{\kappa, \text{measured}}$, across bins of r -band apparent magnitude, redshift, and true galaxy half-light radius in Figure 4 to check the dependence of measurement uncertainty on key physical properties. The results show that $\sigma_{\kappa, \text{measured}}$ slightly increases towards fainter magnitudes, varies modestly with redshift, and tends to decrease with larger true galaxy sizes. Note that our measurements assume a simplified single-component model for all galaxies, consistent with the image simulation inputs. The spike features in the lower two panels of Figure 4 are interpreted as random fluctuations in bins with small numbers of simulated galaxies.

We then compute the uncertainty per redshift bin. The results are shown in Table 1. Across all redshift bins, the measurement scatter in galaxy sizes is much smaller than the intrinsic size dispersion.

³ <https://smtm-002.lsst.io>

⁴ <https://github.com/GalSim-developers/GalSim/blob/releases/2.7/examples/lsst.yaml>

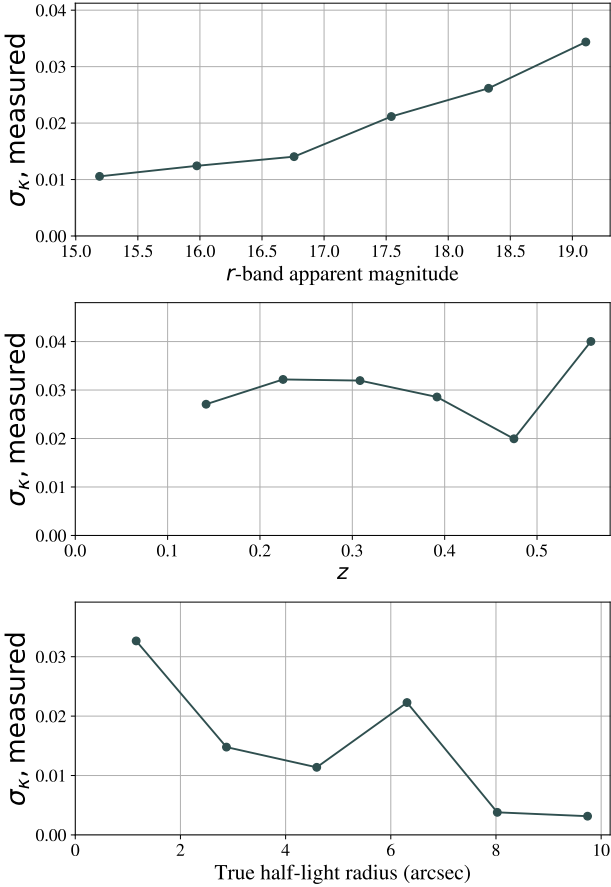


Figure 4. Measurement uncertainty in galaxy half-light radius, σ_κ , measured, with varied r -band apparent magnitude (top), redshift (middle), and lensed half-light radius (bottom), for a sample of 10,000 galaxies from the cosmoDC2 catalogue selected to match DESI BGS-like criteria. Galaxies with $z \leq 0.05$ are excluded from the analysis.

Measurement uncertainties are therefore subdominant, contributing only a small fraction of the total σ_κ .

We have assumed a particular image simulation setup with specific assumptions for image systematic effects, and also a particular galaxy profile fitting approach. All of these aspects could differ in the real LSST images, and the actual analysis will use different profile measurement tools for example. Nevertheless, this is intended to represent a broadly realistic measurement process, with many of the expected complications, and $\sigma_{\kappa, \text{measured}}$ clearly remains sub-dominant to the intrinsic size scatter at all times.

In addition, the fact that the estimator correlates two different fields from different experiments and extracts only a dipole provides further protection against uncorrelated systematics, such as PSF modelling errors, fluctuations in the galaxy number density, or observational variations (e.g. changes in seeing, sky background, blending, or detector response), which are expected to mostly correlate out. In this sense, the Doppler magnification dipole should be quite a robust observable. This should be compared with other measures of peculiar velocities, such as Tully-Fisher/Fundamental Plane, which do require a careful treatment of systematic errors (e.g., [Johnson et al. 2014](#)).

4 FORECASTS

In this section, we quantify the amplitude and detectability of the Doppler magnification dipole for a DESI+LSST-like survey. We adopt the redshift-dependent bias and number density values given in Table 1 of [Andrianomena et al. \(2019\)](#), and construct the covariance assuming an effective overlap sky area of $\sim 5,900 \text{ deg}^2$ ([Olsen et al. 2018](#)). Note that this is an approximate estimate of the overlap, which is likely smaller in practice. However, in the near future, the 4MOST survey will provide an additional overlapping spectroscopic galaxy redshift sample for LSST galaxies ([de Jong et al. 2019](#)). We assume the observed cubic grid has cell size $l_p = 4 \text{ Mpc}/h$.

Figure 5 presents the predicted Doppler magnification dipole $\xi^{\Delta\kappa}(d)$ for the selected DESI+LSST-like sample in four redshift bins, $z \sim [0.15, 0.25, 0.35, 0.45]$, as defined in Section 3.1. The amplitude of the dipole is calculated according to Equation 7. In the figure, the error band is the standard deviation, which is the square root of the diagonal of the covariance matrix (Equation 12). The separation d ranges from 10 Mpc to 310 Mpc, with a uniform bin width of 10 Mpc. For each redshift bin we adopt the corresponding per-bin total galaxy size variation noise values $\sigma_{\kappa, \text{total}}$ from Table 1. The value of $\sigma_{\kappa, \text{total}}$ is computed following Equation 19, where the intrinsic and measurement components are combined in quadrature.

The amplitude of $\xi^{\Delta\kappa}(d)$ is negative across the full range. It drops rapidly for $d \simeq 10\text{--}50 \text{ Mpc}/h$, reaches a broad minimum at $d \simeq 100\text{--}125 \text{ Mpc}/h$, and then turns over, becoming less negative toward larger separations. At fixed separation, the (absolute) amplitude decreases with redshift. The lowest- z bin has the largest (most negative) amplitude. The $1-\sigma$ error bars widen toward large separations for all bins and are broader at low z than at high z . Several factors contribute, including the fact that fewer galaxy pairs exist at large separations, and the comoving volume is smaller at lower z .

Following [Bonvin et al. \(2017\)](#), we define the dipole SNR as

$$\frac{S}{N}(d) = \frac{|\langle \hat{\xi}_{\text{dipole}}^{\Delta\kappa} \rangle(d)|}{\sqrt{\text{cov}[\hat{\xi}_{\text{dipole}}^{\Delta\kappa}](d, d)}}, \quad (24)$$

where $\langle \hat{\xi}_{\text{dipole}}^{\Delta\kappa} \rangle(d)$ is the mean dipole signal at separation d , and $\text{cov}[\hat{\xi}_{\text{dipole}}^{\Delta\kappa}](d, d)$ is the diagonal element of the covariance matrix at d , as described in Equation 12.

Figure 6 shows the dipole SNR in four redshift bins. For all of the bins, the curves peak at small separations, reaching $S/N \simeq 8$ at $z = 0.15$ and $z = 0.25$, and slightly lower values ($S/N \simeq 7$) at $z = 0.35$, near $d \sim 10\text{--}25 \text{ Mpc}/h$. The S/N then declines smoothly with increasing d . At the smallest separations, the lowest z bin has the highest SNR because of the larger dipole amplitude at low redshift. Beyond $d \sim 30 \text{ Mpc}/h$, this trend reverses slightly, likely because larger comoving volumes reduce sample variance and σ_κ declines modestly with redshift, even as the mean number density decreases.

The values remain at a moderate level ($S/N \approx 4\text{--}5$) out to $d \sim 50\text{--}75 \text{ Mpc}/h$. A very shallow increase is visible near $d \sim 90\text{--}125 \text{ Mpc}/h$. By $d \sim 200 \text{ Mpc}/h$, the SNR values for all bins decrease to ≈ 1 . We find that the total S/N per z bin are 12.98, 12.97, 12.66 and 10.41 for $0.1 \leq z < 0.2$, $0.2 \leq z < 0.3$, $0.3 \leq z < 0.4$ and $0.4 \leq z < 0.5$, respectively. We also compute the SNR using the dipole expression in [Bonvin et al. \(2017\)](#) instead of the expression in [Andrianomena et al. \(2019\)](#), and find very similar results. These values are lower than those reported by [Andrianomena et al. \(2019\)](#), mostly because we have a smaller sky area, corresponding to the overlap region between LSST and DESI.

For reference, we show the covariance matrix and the correlation matrix for $\xi^{\Delta\kappa}$ at $0.1 \leq z < 0.2$ in Figure 7. Both the covariance and

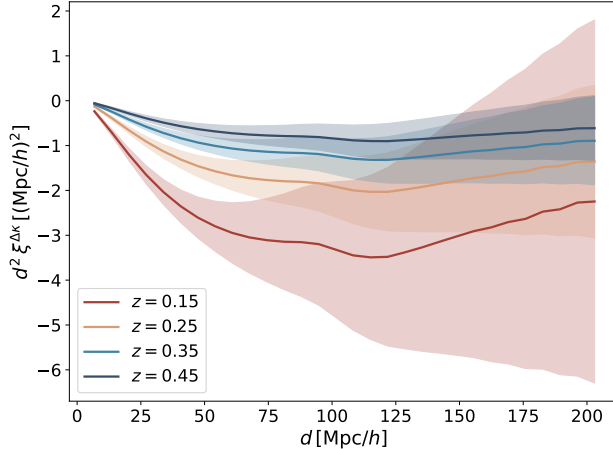


Figure 5. Predicted Doppler magnification dipole $\xi^{\Delta\kappa}$ for a DESI+LSST-like survey in four redshift bins. The solid curves show the amplitude at different redshifts, with shaded regions representing $1-\sigma$ uncertainties from the calculated covariance matrix (Equation 12), computed with the size-noise values $\sigma_{\kappa,\text{total}}$ for each bin from Table 1.

correlation matrices are plotted separately for each of the three terms and for their sum (Equation 12). The correlation matrix is defined as

$$\rho_{ij} = \frac{C_{ij}}{\sqrt{C_{ii} \cdot C_{jj}}}, \quad (25)$$

where C_{ij} represents the covariance between measurements at separations d_i and d_j .

The covariance is largest at the small separations and decreases towards larger d . Once normalized, it is more obvious that the bins at large separations are strongly correlated. Ξ_1 has strong correlations across a wide range of scales and corresponds to the cosmic variance contribution to the signal. Ξ_2 is correlated only for neighbouring separation bins. Ξ_3 is purely diagonal, consistent with being shot noise that does not correlate between different separations. At $d \lesssim 40$ Mpc, Ξ_2 provides the largest contribution to the variance, reflecting the impact of σ_κ . Beyond this scale, Ξ_1 (cosmic variance) dominates, while Ξ_3 remains small at all separations.

Across all redshift bins, Ξ_3 contributes the least among all three components of the covariance (See Figure B1). Towards higher redshifts, the cosmic variance term Ξ_1 contributes less as expected. At the highest two redshift bins, Ξ_2 completely dominates over Ξ_1 at all scales. Additionally, any reduction in σ_κ mainly helps at small separations. Increasing the survey volume through a larger sky area is useful for improving the SNR in the $0.1 \leq z < 0.2$ bin, but has little impact in the higher redshift bins.

5 CONCLUSIONS

We have presented a simulated measurement process and forecasts for detecting the Doppler magnification dipole with a joint DESI+LSST analysis, combining DESI BGS-like galaxy number densities and biases with the convergence field that would be recovered assuming an LSST-informed size-noise model. Using cosmoDC2 to define DESI BGS-like samples, we estimated the per-galaxy size-noise σ_κ per redshift bin. We separated the total σ_κ into intrinsic size dispersion and measurement error. The intrinsic size dispersion was estimated

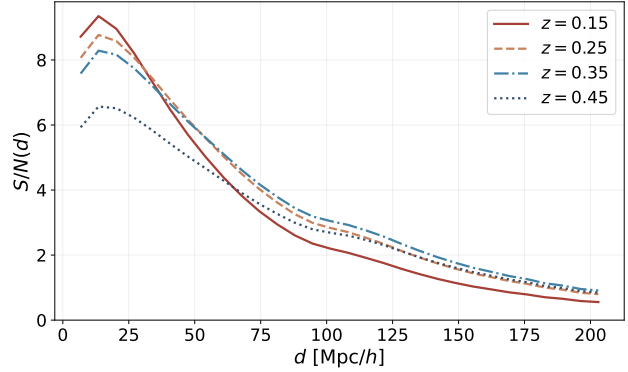


Figure 6. Signal-to-noise ratios of the Doppler magnification dipole for a DESI+LSST-like survey in four redshift bins. The S/N peaks at small separations (~ 10 – 25 Mpc/h) and slowly declines with increasing separation.

directly from the true half-light radii of the simulated galaxies, averaged over the DESI BGS-like population in each redshift bin. We used GALSIM and GALIGHT to generate LSST Y1-quality images and subsequently test the size recovery error. Across all bins, the measurement scatter is well below the intrinsic dispersion under our simplified assumptions, which include single-component Sérsic profiles (fixed n), no ellipticity, and fixed LSST-like PSF/noise configurations. We forecasted detectability by propagating the estimated σ_κ into the covariance for a DESI-area survey, using the Doppler magnification dipole estimator from [Andrianomena et al. \(2019\)](#).

The predicted dipole is negative across all separations, steepens around $d \simeq 10$ – 50 Mpc/h, reaches a broad minimum near $d \simeq 100$ – 125 Mpc/h, and becomes less negative toward larger d . The amplitude decreases with redshift over $z \simeq 0.15$ – 0.45 . The total S/N per z bin is 12.98, 12.97, 12.66 and 10.41 for $0.1 \leq z < 0.2$, $0.2 \leq z < 0.3$, $0.3 \leq z < 0.4$ and $0.4 \leq z < 0.5$, respectively. The corresponding per-bin significance peaks at $S/N \simeq 8$ – 9 around $d \simeq 10$ – 25 Mpc/h, and falls to $S/N \simeq 1$ – 2 by $d \simeq 200$ Mpc/h. Taken together, these results indicate that the dipole should be measured with high significance with this combination of surveys.

From the covariance decomposition, we find that in the lowest redshift bin, the term proportional to σ_κ dominates the variance at small separations and correlates only neighbouring bins. At larger separations, the cosmic variance term became dominant. The purely diagonal shot-noise term contributes the least at all scales. In higher redshift bins, the cosmic variance term decreases significantly, leaving the σ_κ -proportional term as the dominant contribution across nearly all separations. The shot noise-related component remains negligible in all redshift bins. Overall, the total variance is governed by the size noise and cosmic variance, with their relative importance depending on scale and redshift. An increase in the survey volume via a larger survey area would help to enhance the S/N in the lowest redshift bin, but not for the others.

Several caveats should be noted. The simulations presented here are based on a specific LSST-like image setup, and employ a particular galaxy profile fitting approach. Variations in observing conditions, actual sky coverage, and the use of different measurement pipelines could affect the recovered size distributions. In addition, the galaxy sizes in cosmoDC2, which are based on a semi-analytic model and empirical calibration, may not fully reproduce the size distributions that will be observed in real data.

Another caveat is that our galaxy size uncertainty estimates were derived from GALSIM simulations of isolated galaxies and thus do

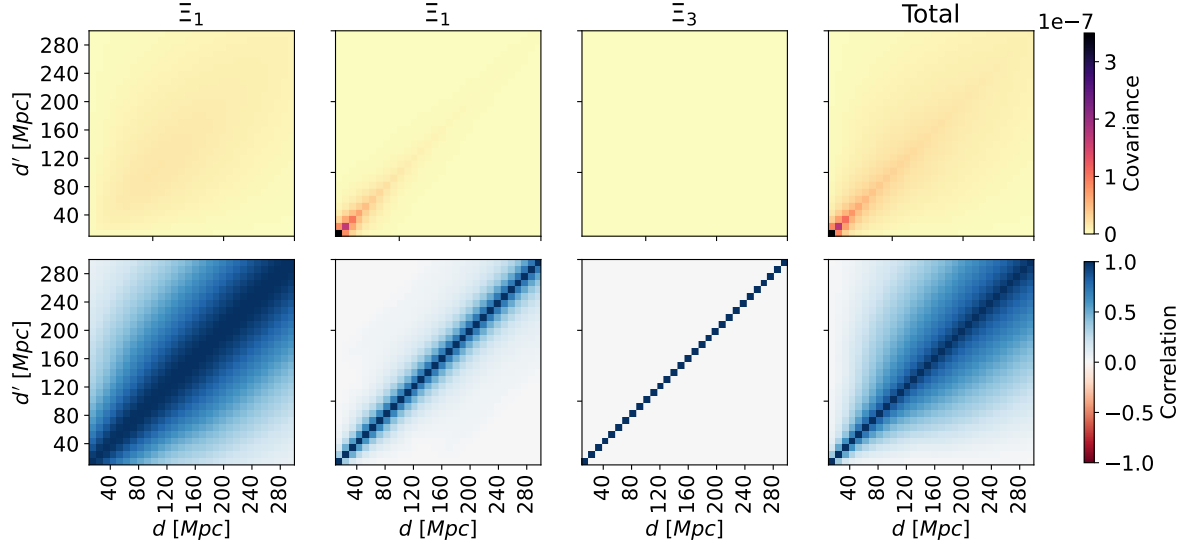


Figure 7. Top panels: Covariance matrices of the Doppler magnification dipole for $0.1 \leq z < 0.2$. The Ξ_1 , Ξ_2 , Ξ_3 , and “Total” panels correspond to the components specified in Equation 12. Bottom panels: The corresponding correlation matrices at $0.1 \leq z < 0.2$ (Equation 25). Axes denote separations d and d' , with bins of width 10 Mpc and axis ticks shown every 40 Mpc for clarity. Each row shares a single colour bar.

not account for the impact of blending. Blending, defined as having at least 1% flux contribution from overlapping neighbours, is expected to affect $\sim 60\%$ of galaxies in 10-year full-depth LSST images (Sanchez et al. 2021), and about 20–30% of objects may be unrecognised blends (Troxel et al. 2023). This reduces the usable galaxy sample and measurement precision. Ignoring such overlapping sources could therefore underestimate the size measurement uncertainties.

As one final note, we also neglected the possibility that other imaging surveys could be used, e.g. the Dark Energy Survey (Dark Energy Survey Collaboration et al. 2016) or DESI’s own legacy imaging surveys (Dey et al. 2019). The latter in particular is, by definition, well-matched with the DESI sample.

In this work, we demonstrated that current and near-future wide-field surveys should be capable of detecting the Doppler magnification dipole. The detectability depends on the effective number density and overlapping volume of the spectroscopic and imaging samples, with performance further conditioned on whether practical requirements (e.g., wide sky coverage, well-modelled PSF and controlled noise) are met. In the DESI+LSST set-up we modelled, intrinsic galaxy-size scatter dominates the size measurement noise, resulting in an adequate S/N for detection at low redshift and a detectable signal across all redshift bins considered.

ACKNOWLEDGEMENTS

We are grateful to A. Nicola for useful comments and discussions. This result is part of a project that has received funding from the European Research Council (ERC) under the European Union’s Horizon 2020 research and innovation programme (Grant agreement No. 948764; P. Bull). I. Ye acknowledges support from the China Scholarship Council (grant no. 202208060318). P. Bull acknowledges support from STFC Grants ST/T000341/1 and ST/X002624/1.

DATA AVAILABILITY

The code used in this study will be publicly available after acceptance.

APPENDIX A: EXAMPLE SIMULATED GALAXY IMAGES

To illustrate the simulated sample used in this analysis, Figure A1 displays a random selection of six example galaxy images generated with GALSIM. These images were drawn from the mock sample based on DESI BGS, and incorporate realistic photometric, atmospheric, and instrumental effects consistent with anticipated LSST observing conditions. Each galaxy was modelled as a Sérsic profile with index $n = 1.5$, convolved with a composite PSF that includes atmospheric Kolmogorov turbulence and optical aberrations (defocus, astigmatism, and coma). Detector noise was added using the expected LSST gain, sky level, and read noise parameters.

APPENDIX B: COVARIANCE DECOMPOSITION

In Section 4, we summarised how different components of the covariance contribute to the total uncertainty of the dipole estimator. For further clarity, Figure B1 shows the redshift and scale dependence of the contributions Ξ_i . These correspond to the cosmic variance term, the σ_κ dependent term, and the shot noise plus σ_κ dependent term (see Equations 13–15).

As shown in the figure, Ξ_2 dominates the cosmic variance at small separations in all bins. Ξ_1 becomes increasingly important at large separations in the lower redshift bins. At higher redshifts, the amplitude of Ξ_1 decreases substantially, leaving Ξ_2 to contribute the most across most scales. The shot noise term Ξ_3 is negligible throughout.

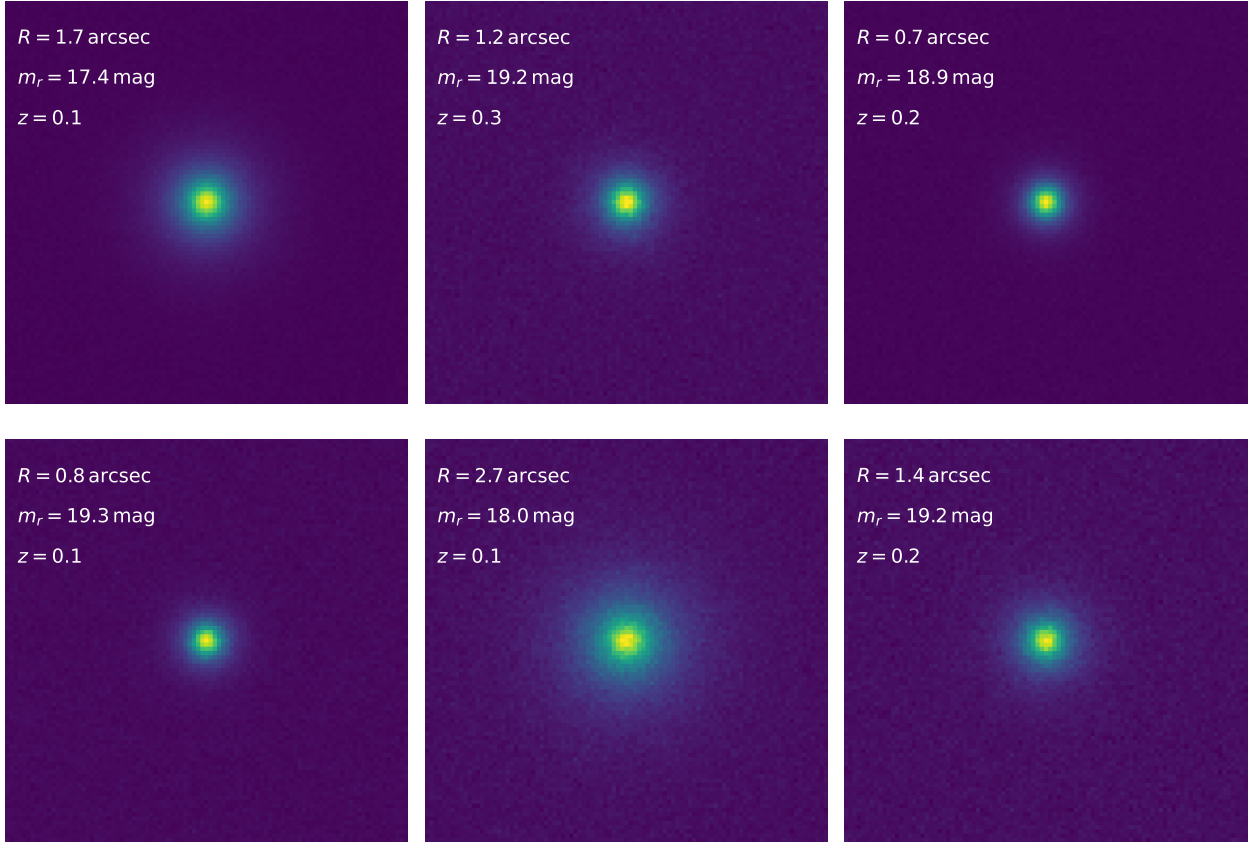


Figure A1. Example simulated LSST galaxy images generated using `GALSIM`. The six panels show galaxies with varying intrinsic half-light radii (R), r -band apparent magnitude (m_r), and z drawn from the BGS sample. The corresponding physical parameters are indicated within each panel. Each galaxy was modelled as a Sérsic profile, and convolved with a atmospheric and optical PSF, including aberrations and detector noise appropriate for LSST observing conditions. The images have a pixel size of $(0.2 \text{ arcsec})^2$, with 95 pixels on each side.

REFERENCES

Allen N., et al., 2025, *A&A*, 698, A30

Alsing J., Kirk D., Heavens A., Jaffe A. H., 2015, *Monthly Notices of the Royal Astronomical Society*, 452, 1202

Andrianomena S., Bonvin C., Bacon D., Bull P., Clarkson C., Maartens R., Moloi T., 2019, *Monthly Notices of the Royal Astronomical Society*, 488, 3759

Bacon D. J., Andrianomena S., Clarkson C., Bolejko K., Maartens R., 2014, *Monthly Notices of the Royal Astronomical Society*, 443, 1900

Benson A. J., 2012, *New Astron.*, 17, 175

Birrer S., et al., 2021, *The Journal of Open Source Software*, 6, 3283

Bonvin C., 2008, *Phys. Rev. D*, 78, 123530

Bonvin C., Durrer R., 2011, *Phys. Rev. D*, 84, 063505

Bonvin C., Andrianomena S., Bacon D., Clarkson C., Maartens R., Moloi T., Bull P., 2017, *Monthly Notices of the Royal Astronomical Society*, 472, 3936

Bonvin C., Lepori F., Schulz S., Tutusaus I., Adamek J., Fosalba P., 2023, *MNRAS*, 525, 4611

Casapona B., Heavens A. F., Kitching T. D., Miller L., Barreiro R. B., Martínez-González E., 2013, *Monthly Notices of the Royal Astronomical Society*, 430, 2844

Challinor A., Lewis A., 2011, *Phys. Rev. D*, 84, 043516

Coates L., Adamek J., Bull P., Guandalini C., Clarkson C., 2021, *Monthly Notices of the Royal Astronomical Society*, 504, 3534

DESI Collaboration et al., 2022, *AJ*, 164, 207

Dark Energy Survey Collaboration et al., 2016, *MNRAS*, 460, 1270

Darragh-Ford E., et al., 2023, *ApJ*, 954, 149

Dey A., et al., 2019, *AJ*, 157, 168

Ding X., et al., 2020, *ApJ*, 888, 37

Djorgovski S., Davis M., 1987, *ApJ*, 313, 59

Dodelson S., Schmidt F., 2020, *Modern Cosmology*, doi:10.1016/C2017-0-01943-2.

Douglas K., 2023, in *APS April Meeting Abstracts*. p. U14.004

Dressler A., Lynden-Bell D., Burstein D., Davies R. L., Faber S. M., Terlevich R., Wegner G., 1987, *ApJ*, 313, 42

Feldman H. A., Watkins R., Hudson M. J., 2010, *MNRAS*, 407, 2328

Gorski K. M., Davis M., Strauss M. A., White S. D. M., Yahil A., 1989, *ApJ*, 344, 1

Hahn C., et al., 2023, *AJ*, 165, 253

Hellwing W. A., Barreira A., Frenk C. S., Li B., Cole S., 2014, *Phys. Rev. Lett.*, 112, 221102

Holz D. E., Hughes S. A., 2005, *ApJ*, 629, 15

Icaza-Lizana M., et al., 2020, *MNRAS*, 492, 4189

Ivarsen M. F., Bull P., Llinares C., Mota D., 2016, *A&A*, 595, A40

Ivezić Ž., et al., 2019, *ApJ*, 873, 111

Johnson A., et al., 2014, *MNRAS*, 444, 3926

Jones R. L., Yoachim P., Ivezić Ž., Neilsen Jr. E. H., Ribeiro T., 2021, Project Science Technical Note PSTN-051, Survey Strategy and Cadence Choices for the Vera C. Rubin Observatory Legacy Survey of Space and Time (LSST), <https://pstan-051.lsst.io/>. NSF-DOE Vera C. Rubin Observatory, doi:10.71929/rubin/2584084, <https://pstan-051.lsst.io/>

Kaiser N., 1987, *MNRAS*, 227, 1

Kennedy J., Eberhart R., 1995, in *Proceedings of ICNN'95 - International Conference on Neural Networks*. pp 1942–1948 vol.4, doi:10.1109/ICNN.1995.488968

Koda J., et al., 2014, *MNRAS*, 445, 4267

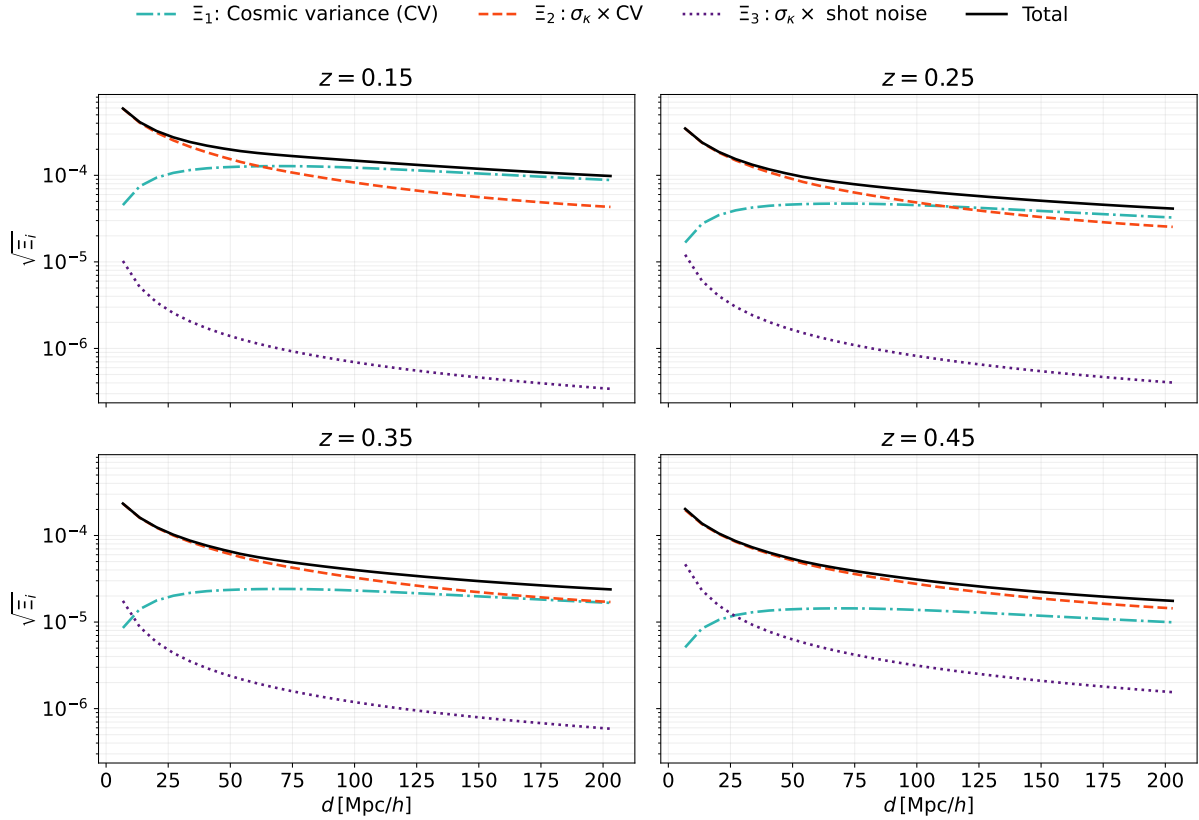


Figure B1. Square root of the diagonal of the covariance contributions $\sqrt{\Xi_i(d)}$ and their total sum, where $i = 1, 2, 3$ (see Equation 12–15), plotted as a function of d for the four redshift bins used in this work.

Korytov D., et al., 2019, *ApJS*, **245**, 26
 LSST Science Collaboration et al., 2009, *arXiv e-prints*, p. arXiv:0912.0201
 Lange R., et al., 2015, *MNRAS*, **447**, 2603
 Lyall S., Blake C., Turner R., Ruggieri R., Winther H., 2023, *MNRAS*, **518**, 5929
 Olsen K., et al., 2018, *arXiv e-prints*, p. arXiv:1812.02204
 Phillips M. M., 1993, *ApJ*, **413**, L105
 Planck Collaboration et al., 2020, *A&A*, **641**, A6
 Rowe B. T. P., et al., 2015, *Astronomy and Computing*, **10**, 121
 Sanchez J., Mendoza I., Kirkby D. P., Burchat P. R., LSST Dark Energy
 Science Collaboration 2021, *J. Cosmology Astropart. Phys.*, **2021**, 043
 Saulder C., et al., 2023, *MNRAS*, **525**, 1106

Shen S., Mo H. J., White S. D. M., Blanton M. R., Kauffmann G., Voges W.,
 Brinkmann J., Csabai I., 2003, *MNRAS*, **343**, 978
 Troxel M. A., et al., 2023, *MNRAS*, **522**, 2801
 Tully R. B., Fisher J. R., 1977, *A&A*, **54**, 661
 Turner R. J., 2024, *arXiv e-prints*, p. arXiv:2411.19484
 Zarrouk P., et al., 2018, *MNRAS*, **477**, 1639
 Zhang Y.-C., Yang X.-H., 2019, *Research in Astronomy and Astrophysics*,
19, 006
 de Jong R. S., et al., 2019, *The Messenger*, **175**, 3
 van der Wel A., et al., 2014, *ApJ*, **788**, 28

This paper has been typeset from a $\text{\TeX}/\text{\LaTeX}$ file prepared by the author.